Chemical Science

Accepted Manuscript

This article can be cited before page numbers have been issued, to do this please use: M. Lian, Y. Sun, D. Zhou, Y. Zhang, Q. Zhou, Y. Jiang and Z. Ye, *Chem. Sci.*, 2026, DOI: 10.1039/D6SC03276A.

ROYAL SOCIETY OF CHEMISTRY

rsc.li/chemical-science

View Article Online
DOI: 10.1039/D6SC03276A

Mingyu Lian,[a] Yitong Sun,[b] Di Zhou,[b] Yijia Zhang,[a] Qingqing Zhou,[b] Ying Jiang,[b,*] Zhengqing Ye[a,c,*]

[a]Tianjin Key Laboratory of Materials Laminating Fabrication and Interface Control Technology, School of Material Science and Engineering, Hebei University of Technology, Tianjin 300401, P.R. China

[b]School of Material Science and Engineering, Tianjin University of Technology, Tianjin 300384, P.R. China

[c]Joint Key Laboratory of the Ministry of Education, Institute of Applied Physics and Materials Engineering, University of Macau, Avenida da Universidade, Taipa, Macau SAR 999078, P.R. China

*Corresponding author: yingjiang@email.tjut.edu.cn, zqye@hebut.edu.cn

DOI: 10.1039/D6SC03276A

Synergetic Electronic Spin Modulation and Asymmetric Orbital Hybridization at $CoSe_2/Fe_3Se_4$ Interface Inducing Robust SEI for Enhanced Sodium Ion Storage

View Article Online
10.1039/D6SC03276A

Keywords: electronic spin modulation, asymmetric orbital hybridization, heterostructure design, solid electrolyte interface modulation, sodium-ion batteries

Abstract:

Transition metal selenides (TMSes) are recognized as promising anode materials for sodium-ion batteries (SIBs) owing to their ideal capacity and low cost, but their practical application suffers from crucial issues of inferior cycling stability and sluggish reaction kinetics. Herein, we design a magnetic $CoSe_2/Fe_3Se_4$ (CFSE) heterostructure to simultaneously regulate orbitals and spin features, aiming to systematically reveal their synergistic effect on sodium-ion storage. The orbital spin splitting of CFSE heterostructure drives the Co^{2+} spin state transition from low to high, which improves the adsorption energy and lowers the diffusion energy barrier of sodium ions. Meanwhile, Co−Se−Fe asymmetric orbital hybridization promotes a charge transfer pathway at the interface and ensures the directional migration of ions, thereby inhibiting irreversible structural variations, and tailoring an ultrathin and robust SEI film during battery operation. As a result, the as-prepared CFSE electrodes achieve a high reversible capacity of 395.8 mAh g^{-1} at 2.0 A g^{-1} over 1200 cycles and deliver an excellent rate stability of 364.4 mAh g^{-1} at 10.0 A g^{-1}. This work provides an in-depth understanding of the spin-orbit modulation mechanism and inspiration for developing advanced conversion-type anodes.

View Article Online
DOI: 10.1039/D6SC03276A

Introduction

In the pursuit of sustainable energy storage systems, sodium-ion batteries (SIBs) have emerged as a promising alternative to lithium-ion batteries (LIBs) owing to the abundant sources, cost-effectiveness, and environmental compatibility.[1-3] However, SIB anodes face severe challenges, including the large ionic radius of Na^+ (1.02 Å) compared to Li^+ (0.76 Å), which results in sluggish diffusion kinetics, thus leading to poor rate capability of SIBs.[4-9] Therefore, great efforts have been devoted to developing high-rate anode materials for extending the potential application of SIBs. Among them, transition metal selenides (TMSes) have garnered substantial attention owing to their high theoretical capacity and outstanding rate performance originating from their multi-step electronic conversion reactions and narrow bandgap structures.[10-13] Nevertheless, the development of TMSes has been impeded by the low intrinsic electronic conductivity and slow ion diffusion kinetics. In addition, they also suffer from unfavorable volume variations during discharge/charge cycling, which leads to the repeated breakage/re-formation of solid electrolyte interphase (SEI) film, thus deteriorating the cycling life.

In this respect, the heterostructure engineering can spontaneously generate a built-in electric field (BIEF) at two phases interface, which exhibits favorable charge transfer and ion diffusion dynamics.[14-20] Among them, bimetallic selenide heterostructures including Sb_2Se_3/WSe_2,[21] $Se{-}CoS_2/CoSe_2$,[22] and $MoSe_2/Bi_2Se_3$[23] have gained significant attention owing to their ability to promote fast and durable sodium storage during discharging and charging processes. For instance, Ge et al. developed a

View Article Online
DOI: 10.1039/D6SC03276A

microcrystalline-$MoSe_2$/amorphous-$MoSe_xO_y$ (C-$MoSe_2$/A-$MoSe_xO_y$) heterostructure, which shows an ultrahigh specific capacity and rate performance for SIBs.[24] The improved performance is attributed to the charge self-modulation effect at the microcrystalline-amorphous heterogeneous interface in C-$MoSe_2$/A-$MoSe_xO_y$. This activates Mo−Se bonds and modulates the interfacial charge rearrangement, thus significantly enhancing sodium ion adsorption and electron/ion transport. Li et al. successfully designed a CoSe/$MoSe_2$ heterostructure integrated with homogeneous carbon composites (CoSe/$MoSe_2$-C) through solvothermal methods, followed by selenization and carbonization processes.[25] As expected, the CoSe/$MoSe_2$-C shows a high capacity and ultra-long lifespan in sodium-ion half/full batteries. The construction of heterostructure can regulate the charge redistribution at the heterointerface by virtue of the BIEF effect, which reduces the energy barrier for ion diffusion and enhances charge transfer kinetics. However, considering the spin-sensitive characteristic of sodium storage reactions, there is a critical need to develop new types of heterostructures that can modulate spin states in TMSes.

Spin represents an additional intrinsic property of electrons, and often plays an essential role in the electronic configuration of the active site, further optimizing sodium ion adsorption energy during battery operation.[26] For example, Li et al. proposed an electronic-spin regulation in $CoSe_2$/$MoSe_2$ heterostructure toward fast and stable sodium storage.[27] The introduced Mo cations within the $CoSe_2$/$MoSe_2$ not only serve as electron donors to modulate charge-spin configurations with rich active electronic states but also lead to the upshift of *d*/*p* band centers and the reduction of

View Article Online
DOI: 10.1039/D6SC03276A

Δ*d*–*p* band center gap, thus improving sodium ion adsorption capacity and decreasing the ion diffusion barrier. Sikandar Iqbal et al. introduced a competitive coordination approach to fabricate Se-rich ZnSe/MnSe heterostructure, enabling high reversibility for sodium ion storage.[28] In particular, *p* orbitals of Se push a shift from high spin to low spin state of Mn *d*-orbitals, which accelerates charge migration from ZnSe to MnSe. This provides rich sites for sodium ion insertion/de-insertion, and accommodates volume expansion, which in turn improves the reversibility of anode materials during cycling. Consequently, constructing unique TMSe heterostructures to concurrently modulate both electron density and spin state is expected to be an effective way to improve electrochemical performance of SIBs. Although spin engineering helps understand the origins of favorable sodium storage performance in heterostructures, the spin state modulation mechanism remains unclear. Moreover, the interplay of spin and orbital at the heterointerface can tailor the atomic coordination environment and electronic structure compared to their bulk counterparts, resulting in unique physicochemical characteristics.

Herein, we prepared a magnetic $CoSe_2/Fe_3Se_4$ (CFSE) heterostructure with synergistic regulation of spin state and orbital hybridization, intending to systematically reveal their synergistic influence on sodium ion storage. Theoretical calculation demonstrates that the orbital spin splitting of CFSE heterostructure induces a spin-state transition in Co^{2+} (from low-spin to high-spin), which results in the upshift in the *d* band center (ε_d) of Co, thus optimizing the adsorption energy and stabilizing Na-intercalated phase. Meanwhile, an asymmetric Co–Se–Fe orbital hybridization at the

View Article Online
DOI: 10.1039/D6SC03276A

heterointerface leads to the generation of an electronic transport pathway, promoting charge transport from Fe to Co, and lowering the diffusion barrier for Na^+, thereby improving the electrochemical reaction kinetics of CFSE. Moreover, CFSE heterostructure reduces the dissociation energy barrier of $NaPF_6$, inducing an even and inorganic-rich component SEI film to improve structural stability. Ultimately, the CFSE electrodes achieve fantastic electrochemical performances for sodium storage compared to those of pristine individual components.

Results and discussion

To study the effect of heterostructure on the electronic structures, total density of states (TDOS) and partial density of states (PDOS) of three samples are calculated. The DOS results show that CFSE possesses larger density states at the Fermi level (E_f) compared with $CoSe_2$ (CSE) and Fe_3Se_4 (FSE), suggesting better electronic conductivity, which is beneficial for charge transport during redox reaction processes (Fig. S1). In addition, the PDOS results reveal that the electronic states of Fe-*d* orbitals in FSE and Co-*d* orbitals in CSE show an asymmetry characteristic, which originates from the uneven arrangement of electrons in spin-up and spin-down (Fig. S2). In comparison, this asymmetry of Fe-*d* orbitals and Co-*d* orbitals in CFSE is stronger (Fig. 1a,b), thus leading to more spontaneous spin polarization. This result indicates that CFSE can offer spin-polarized electrons, which are conducive to adsorbing sodium ions. Furthermore, there are changes in the electron-donor or electron-acceptor characteristics of the coordination environment in CFSE by virtue of the introduction of spin state manipulation as well as an improvement of Co *d* band centers (Fig. S3).

View Article Online
DOI: 10.1039/D6SC03276A

Moreover, the energy levels of $3d_{yz}$, $3d_{xz}$, $3d_{xy}$, $3d_{x^2-y^2}$, and $3d_{z^2}$ are plotted respectively according to their *d* band centers (Fig. 1c and Fig. S4). For Co-*d* spin up orbitals, the $3d_{z^2}$ is the highest occupied orbital in CSE, while the $3d_{xz}$ is the highest occupied orbital in CFSE. Notably, the construction of heterostructures can significantly influence the highest occupied orbitals of active metal atoms owing to the orbital hybridization and charge transport across the heterointerface.[29] It is considered that the electrons occupied in orbital near the E_f possess higher reactivity. Therefore, the highest occupied *d* orbital plays a significant role in modulating the adsorption behavior of intermediates. Furthermore, the PDOS for three samples were simulated to investigate electron contributions from various Co-3*d* orbitals and Fe-3*d* orbitals (Fig. 1d,e). In CSE, 39.8% and 40.7% of electrons in the $d_{x^2-y^2}$ and d_{z^2} orbitals are unpaired, while 34.1%, 36.3%, and 46.6% of electrons in d_{xy}, d_{xz}, and d_{yz} orbitals are unpaired. Moreover, in CFSE, 62.5% and 79.9% electrons in the $d_{x^2-y^2}$ and d_{z^2} orbitals are unpaired, and 53.7%, 72.2%, and 74.3% electrons are unpaired in the d_{xy}, d_{xz}, and d_{yz} orbitals, respectively. Thus, the probability of identifying a Co^{2+} in $t_{2g}^5e_g^2$ high electronic spin state is higher in CFSE than in CSE.

To further confirm the charge regulation effect of the active Fe−Se and Co−Se bonds at the heterointerface, differential charge density was calculated. The green regions indicate electron depletion, while the orange regions represent electron accumulation. The heterointerface coupling allows electron redistribution and the generation of BIEF, which is further substantiated by the quantized electron distribution along the Z-axis direction (Fig. 1f). The observed peaks located at the interlayer

View Article Online
DOI: 10.1039/D6SC03276A

positions confirm the substantial charge transfer at the heterointerface, indicating obvious charge redistribution. Electron localization function (ELF) results demonstrate reduced electron localization on Se atoms in CFSE compared with pristine FSE (Fig. 1g and Fig. S5), which is consistent with predominant charge transfer from Fe_3Se_4 to $CoSe_2$. The charge redistribution near the CFSE interface and the electron depletion and accumulation among different atoms were quantified via Bader charge analysis (Fig. 1h). Bader charge analysis indicates that the $CoSe_2$ unit gains 0.78 electrons from the Fe_3Se_4 structure.[30] The generation of BIEF induces space charge redistribution, which is expected to be an effective approach to manipulate spin states, thus accelerating Na^+ migration and enhancing the rate performance of SIBs.[24] To elucidate the intrinsic driving mechanism of electron transfer at the interface, the work function value (Φ) of different samples were further obtained by DFT calculation (Fig. 1i and Fig. S6). The Φ of CFSE (4.45 eV) is the lowest, which indicates that electrons on the heterostructure surface are the easiest to transfer, enabling CFSE to have superior electrical conductivity. In addition, FSE shows a lower Φ of 4.60 eV compared to 5.18 eV for CSE, facilitating a spontaneous electron flow from FSE to CSE at the heterointerface, thereby generating a BIEF from FSE to CSE that significantly accelerates reaction kinetics and reversible insertion/extraction process of Na ions (Fig. 1j).

The adsorption energy values and corresponding structure models of Na^+ on the surface of CFSE, CSE, and FSE are shown in Fig. 1k and Fig. S7. Notably, the CFSE heterostructure exhibits a more negative Na adsorption energy (−3.79 eV) than

View Article Online
DOI: 10.1039/D6SC03276A

individual CSE (−2.79 eV) and FSE (−2.90 eV), indicating that heterostructure construction can induce stronger adsorption of Na atom and thermodynamically more favorable Na adsorption.[31] The bonding strength of Na−Se was further investigated through Crystal Orbital Hamilton Population (COHP) analysis. The negative and positive values of COHP signify bonding and antibonding states, respectively. The bonding states of CFSE are mostly below the E_f with more occupations, while the bonding states of CSE and FSE shift below the E_f with fewer occupations. Furthermore, the integrated COHP (ICOHP) was calculated to directly quantify the bonding strength. The CFSE exhibits a more negative ICOHP value (−0.38 eV) than those of CSE (−0.30 eV) and FSE (−0.31 eV), confirming its stronger chemical bond (Fig. S8).

COHP analysis also is employed to assess the bonding stability of the corresponding Na-intercalated phase. The ICOHP value in Na-intercalated CFSE (−0.99 eV) is markedly more negative than that of pristine CFSE (−0.94 eV), indicating substantially enhanced thermodynamic stability after Na intercalation (Fig. 1l). The reaction kinetics are further analyzed. Fig. 1m shows the diffusion paths of sodium ions and corresponding diffusion energy barriers in three materials (Fig. S9). The results indicate that CFSE has the lowest diffusion barrier for sodium ions, of only 0.31 eV, suggesting a relatively fast migration of sodium ions within CFSE. This improves electrochemical reaction dynamics, thus implying the potential for CFSE to achieve exceptional electrochemical properties.[32]

Notably, CFSE exhibits the highest Na^+ binding energy and the smallest Na^+ diffusion barrier. This is primarily caused by its unique electronic structure (Fig. 2a).

View Article Online
DOI: 10.1039/D6SC03276A

PDOS analysis results demonstrate that the electron structure of Co cations in CSE are the low spin state ($t_{2g}^6e_g^1$). In contrast, Co cations in CFSE possess a valence electron configuration of $t_{2g}^5e_g^2$ with a high spin state (Fig. 2b). More specifically, the valence electron configuration of Co^{2+} in CSE is $3d^7$ with fully occupied π-symmetry (t_{2g}) orbitals. Consequently, electron repulsion emerges as the primary interaction between bridging Se and Co. In contrast, the π-symmetry orbitals of Co^{2+} in CFSE are half-empty, allowing interaction with bridging Se via π-donation.[33] The electronic configuration of Fe^{2+} can be described as $t_{2g}^4e_g^2$ in the CFSE and FSE, which are unpaired for the high spin state of Fe^{2+}. The interaction between Fe^{2+} and Se is implemented through the π-donation.[34] In addition, the effect of Co and Fe on Se site activity can be assessed through covalent character.[35] The covalent characters of Fe−Se and Co−Se bonds are 87.8% and 89.4%, respectively (Fig. S10). The higher covalent character indicates that the metal 3*d* orbitals have a stronger electron withdrawing ability, which results in charge transfer between Se sites and metal atoms. CFSE possesses a stronger π-donation interaction of Co−Se than that of Fe−Se counterpart, thus leading to partial transfer of Fe electron to Co via asymmetric orbital hybridization within the Co−Se−Fe bridging configuration. The Co−Se−Fe asymmetric orbital hybridization at the heterostructure drives electron redistribution and regulates electron-spin state in the metal center, resulting in the upshift in the ε_d of Co (Fig. S3). Moreover, Se atoms in CFSE possess the highest *p* band center (ε_p) among all samples (Fig. S11), thus reducing the occupancy degree of the Na−Se antibonding sigma orbital (σ^*) (Fig. 2c). This result improves the interaction between Na^+ and Se in the metal selenide heterostructure,

View Article Online
DOI: 10.1039/D6SC03276A

thereby enhancing adsorption energy toward Na^+.[36]

Inspired by theoretical calculations, the CFSE anode material was successfully constructed by a simple two-step strategy of co-precipitation and selenization (Fig. S12). The selected-area electron diffraction (SAED) pattern exhibits the presence of the (023), (210), and (111) planes of $CoSe_2$ as well as (103), (105), and (015) crystal planes of Fe_3Se_4 (Fig. 2d). This confirms the generation of CFSE heterostructures. In the high-resolution transmission electron microscopy (HRTEM) of CFSE images in Fig. 2e, the marked lattice spacings of 0.54 and 0.55 nm correspond to the (101) and ($\bar{1}$01) planes of Fe_3Se_4 (Fig. 2f,g). Additionally, the CFSE features d-spacings of 0.19 and 0.23 nm, corresponding to the (221) and (211) planes of $CoSe_2$ (Fig. 2h,i). The presence of heterojunction was further confirmed by high-angle annular dark-field scanning TEM (HAADF-STEM) and corresponding elemental mapping analysis (Fig. 2j), revealing the uniform distribution of cobalt, iron, and selenium elements in CFSE.

To further investigate the influence of heterostructure design in ion diffusion kinetics and mechanical stress distribution, the finite element analysis was employed. Two different models were constructed: 1) a heterostructure of CFSE composite (Uniformly dispersed CSE-inserted particles were fabricated on FSE substrate), and 2) a control model of CSE or FSE with a single particle phase. The sodium ion concentration of both systems at various sodiation states is investigated. The single-phase particles show a larger radial sodium ion concentration gradient compared to the heterostructure during discharging (Fig. 2k,l), indicating that the single-phase particles are prone to localized concentration accumulation. Specifically, surface-preferential

View Article Online
DOI: 10.1039/D6SC03276A

Na^+ insertion during discharging establishes a Na^+ concentration gradient, inducing substantial mismatch strain at the bulk-surface interface. The single CSE or FSE system, featured by slow surface diffusion dynamics, exhibits incomplete bulk sodiation and gradual stress accumulation (Fig. 2l,n). In contrast, the CFSE exhibits highly efficient and even bulk-surface kinetics, significantly alleviating concentration polarization and associated mechanical stress (Fig. 2k,m). Therefore, strategic regulation of surface Na^+ transport kinetics by compositional heterostructure engineering provides a significant approach for achieving improved diffusion dynamics throughout the whole particle in anode materials.

X-ray diffraction (XRD) was used to investigate the crystalline phase structure of the as-synthesized CFSE samples. As shown in Fig. 3a, the CFSE exhibits representative diffraction peaks at 33.5°, 51.7°, and 56.6°, corresponding to the (202), (310), and ($\bar{1}$16) planes of the phase Fe_3Se_4 (PDF no. 71–2251). Meanwhile, three dominant peaks located at about 34.2°, 37.6°, and 51.7° refer to the (210), (211), and (311) planes of $CoSe_2$ (PDF no. 89–2002). The XRD analysis results confirm the successful preparation of the CFSE. X-ray photoelectron spectroscopy (XPS) was employed to explore the surface compositions and chemical bonding states in three samples (Fig. 3b-d). The survey spectra of CFSE samples exhibit the presence of Fe, Co, O, N, C, and Se elements (Fig. S13). Specifically, the Co 2p spectra (Fig. 3b) of CFSE exhibited two peaks of 799.9 and 782.0 eV, which are attributed to Co^{2+} $2p_{1/2}$ and Co^{2+} $2p_{3/2}$, respectively. The peaks at 779.5, 795.7, 802.4, and 785.4 eV are ascribed to the $2p_{3/2}$ and $2p_{1/2}$ of Co^{3+} and two satellite peaks, respectively.[37] In comparison to

View Article Online
DOI: 10.1039/D6SC03276A

CSE, the Co 2p peak of CFSE exhibits a shift toward lower binding energy, which could be attributed to the formation of a BIEF within the heterostructure, suggesting that the charge transfer results from the rearrangement of electron cloud density of robust synergistic coupling between $CoSe_2$ and Fe_3Se_4.[38, 39] The Fe 2p XPS spectra (Fig. 3c) of CFSE can be divided into six distinct peaks, where the peaks emerging at 713.9 and 727.8 eV are assigned to $2p_{3/2}$ and $2p_{1/2}$ of Fe^{3+}, while the peaks centered at 710.4 and 723.7 eV belong to Fe^{2+} $2p_{3/2}$ and Fe^{2+} $2p_{1/2}$, respectively. Additionally, two remaining peaks located at 717.9 and 732.2 eV correspond to satellite peaks.[40] The positive shift of the Fe 2p peak results from the valence structure reconstruction induced by the incorporation of $CoSe_2$, which indicates the reduction of valence electrons compared to the E_f and downshift of the *d* band center. In the high-resolution Se 3d spectra (Fig. 3d and Fig. S14), two distinct peaks located at 53.8 and 55.1 eV are attributed to the Se $3d_{5/2}$ and Se $3d_{3/2}$, respectively. The peak at 57.6 eV is associated with the Se−C bonding configuration. The peak observed at 58.8 eV corresponds to SeO_x species, resulting from the oxidation of Se^{2-} under air conditions.[41]

To further identify the generation of the Co−Se−Fe bond, the detailed structures of CSE, CFSF, and FSE were analyzed by X-ray absorption spectroscopy (XAS) characterization. Compared with CSE (Fig. 3e), the X-ray absorption near-edge structure (XANES) of Co K-edge in CFSE moves to a lower energy, demonstrating the increased electron density on Co atoms due to heterostructure effect, which corresponds well with the XPS and DFT results. Nevertheless, the near-edge characteristics of Fe K-edge in CFSE are obviously different from those of the Co K-edge counterpart,

View Article Online
DOI: 10.1039/D6SC03276A

implying an elevated oxidation state of Fe species (Fig. 3g). In addition, the weakened peak intensity of the white line near 7720 eV (Fig. 3e) indicates that the white line peak intensity is associated with the spin state of metal atoms and the coordination environment.[42] Specifically, Co^{2+} exhibits a higher spin state in the CFSE than that of CSE.

The Fourier transformed extended X-ray absorption fine structure (FT-EXAFS) spectra of CFSE show a dominant peak at 2.21 Å, corresponding to the first shell Co–Se coordination. The Co−Se coordination in CFSE exhibits a low shift of the characteristic peak compared to CSE, which can be attributed to the reduced bond length. This result indicates enhanced coordination interaction between Co and Se in CFSE, which is consistent with DFT calculation results. The lower peak intensities could originate from interfacial lattice disordering of CFSE. An obvious weakening in the intensity of the Co−Se peak for CFSE compared with CSE (Fig. 3f) suggests a lower coordination number that is likely related to the variation of spin state in the CFSE (Fig. S15 and Table S1). However, the peak intensity of Fe−Se coordination located at about 2.20 Å in CFSE is higher than that in FSE, indicating a higher Fe−Se coordination number after introducing heterostructure engineering (Fig. 3h). The high radical distance shift of the Fe−Se peak in the CFSE could be attributed to the generation of strongly coupled interfaces between $CoSe_2$ and Fe_3Se_4.

Moreover, the k^3-weighted wavelet transform (WT) contour plot is utilized to further validate the local coordinated environment of CSE, CFSE, and FSE, respectively (Fig. 3i-l). In contrast to CSE, the WT contour plots of CFSE exhibit a

View Article Online
DOI: 10.1039/D6SC03276A

minor shift to the right direction, indicating that there exists electron transfer between Fe_3Se_4 and $CoSe_2$ to promote the sodium-ion adsorption/desorption processes (Fig. 3i,j). Similarly, the maximum intensity of FSE centers at k = 5.33 $Å^{-1}$, while the highest intensity in CFSE exhibits an obvious positive shift (Fig. 3k,l). This result further demonstrates that the BIEF in the CFSE heterogeneous interface leads to the variation of Fe electron configuration. Interestingly, the notably greater intensity of Fe−Se in CFSE compared to FSE reveals an augmented coordination number. The above results indicate the successful modulation of the local coordination environment for the Co and Fe sites in CFSE by the BIEF within the heterostructure.

To further study the electrochemical reaction process within the three samples, the cyclic voltammetry (CV) curves at different scan rates from 0.2 to 1.0 mV s^{-1} were measured. As illustrated in Fig. 4a, the CV curves of CFSE exhibit excellent similarity in peak positions and shapes within the voltage range of 0.01 to 3.0 V at various scan rates, demonstrating the superior conversion reaction kinetics of the heterostructure during charge and discharge processes. The correlation between the peak currents and different scan rates is calculated.[15] The electrochemical kinetic behavior during discharge/charge processes can be evaluated by the *b* values. Fig. 4b reveals that the *b* values for the anodic and cathodic peaks of CFSE are 0.93 (A1), 0.97 (A2), 0.87 (A3), 0.95 (C1), and 1.08 (C2), respectively, which are approximately close to 1.0, suggesting the predominance of the pseudocapacitive reaction mechanism for SIBs based on the CFSE electrode.[38] Furthermore, the *b* values for pristine CSE and FSE are both about 1.0 (Fig. S16 and S17), indicating the dominant pseudocapacitive contribution of the

View Article Online
DOI: 10.1039/D6SC03276A

composite structure. Notably, the *b* values of CSE and FSE are obviously smaller than that of CFSE, indicating that despite pseudocapacitive behavior is dominant, the diffusion-controlled contributions cannot be ignored (Fig. S18). Additionally, CFSE displays a higher pseudocapacitive contribution (96%) than that of CSE (88%) and FSE (95%) at a scan rate of 1.0 mV s^{-1} (Fig. S19).[43] Furthermore, CFSE shows higher capacitive contribution ratios than those of CSE, FSE electrodes at all investigated scan rates (Fig. 4c). These results indicate excellent charge storage kinetics of CFSE anodes, which is conducive to its superior rate capability and long-cycle stability.

The ion diffusion coefficient is a crucial factor that directly reflects the dynamics of electrochemical reactions. To further assess the Na^+ diffusion coefficient (D_{Na^+}) for CFSE, CSE, and FSE electrodes, the galvanostatic intermittent titration technique (GITT) was conducted at a current density of 0.1 A g^{-1} (Fig. S20).[44] As a result, CFSE shows a higher average D_{Na^+} value compared with CSE and FSE during the discharge/charge process (Fig. 4d), suggesting dominance of rapid Na^+ intercalation/extraction processes at the electrode-electrolyte interface. In addition, the activation energy (E_a) for all electrodes can be further calculated by the Arrhenius equation.[38, 45] An optimal equivalent circuit is adopted to perform simulations of a series of collected electrochemical impedance spectroscopy (EIS) spectra to evaluate specific resistance (Fig. S21 and Fig. S22).[46, 47] The E_a value of CFSE (10.79 kJ mol^{-1}) is smaller than those of CSE (26.39 kJ mol^{-1}) and FSE (29.17 kJ mol^{-1}), demonstrating that the energy barrier of the Na^+ desolvation in CFSE is relatively lower compared with CSE and FSE, which promotes the Na^+ intercalation into CFSE.[40]

View Article Online
DOI: 10.1039/D6SC03276A

In-situ EIS was employed to elucidate Na^+ transfer kinetics of CFSE electrodes. The EIS profiles exhibit two overlapping semicircles and a line at high, medium, and low frequency ranges, which correspond to the Na^+ diffusion in SEI (R_{SEI}), charge transfer resistance (R_{ct}), and Warburg impedance (Z_w), respectively (Fig. S23). The semicircular arc of the CFSE electrode in the high-frequency ranges (Fig. S24) shows an obvious shrinkage during discharge process and then maintains stable during charge stage, indicating effective charge carrier transfer of CFSE anodes. In contrast, the semicircular arc of the CSE exhibits a disordered state in the initial discharge process, illustrating slow charge transport and an unstable interface. It is noticed that R_{SEI} and R_{ct} for the CFSE electrode have been significantly reduced when compared to those in CSE and FSE electrodes (Fig. S24-26), revealing that the spin-modulated CFSE heterostructure can significantly accelerate reaction kinetics of Na^+ across the SEI layer and Na^+ transport from electrolyte to the electrode.[48]

To accurately distinguish various electrochemical processes, in-situ EIS were further analyzed utilizing the distribution of relaxation times (DRT) technique (Fig. 4e-g). According to the timescale investigation, the peaks predominantly center at $\tau_1=10^{-5}$, $\tau_2=10^{-4}\sim10^{-2}$, $\tau_3=10^{-2}\sim1$, and $\tau_4=1\sim2$ s, which correspond to the Ohmic resistance (R_s), R_{SEI}, R_{ct}, and Z_W, respectively. Across τ_1-τ_3 timescales, the CFSE shows smaller peak intensities and excellent cycling stability than that of CSE and FSE. In particular, the τ_2 peak of CSE and FSE is initially large and drops after the subsequent discharge stage, which is attributed to uneven and thick SEI formation during electrochemical process (Fig. S25 and Fig. S26). In contrast, the τ_2 peak is considerably smaller and more stable,

View Article Online
DOI: 10.1039/D6SC03276A

indicating an even and thin SEI film formation in CFSE electrode material. Notably, there are two distinct R_{ct} peaks observed, confirming that the electrochemical reaction of CFSE is a multi-electron reaction (Fig. S24). The τ_3 peaks for CFSE are smaller than those of CSE and FSE, which indicates superior Na^+ transport kinetics and enhanced electronic conductivity (Fig. S27). During discharging stage, the intensity of the τ_3 peaks for CFSE progressively decreases, accompanied by a more obvious reduction in relaxation time than those of CSE and FSE, suggesting accelerated interfacial kinetics via spin-driven heterostructure.

To illustrate the impact of heterostructure construction and spin modulation on electrochemical performances, the CV curves of CFSE at 0.1 mV s^{-1} between 0.01 and 3.0 V were investigated (Fig. S28). During the first cathodic scan, a reduction peak at ≈1.35 V is detected, which is owing to the insertion of sodium ions into CFSE ($CoSe_2/Fe_3Se_4 + xNa^+ + xe^- \rightarrow Na_xCoSe_2/Fe_3Se_4$). Subsequently, the cathodic peaks located at ≈1.13 and 0.69 V can be attributed to the conversion reaction of Na-intercalated phase to metal Co, Fe, and Na_2Se as well as the formation of the SEI film, respectively. A pair of redox peaks near 0.01 V stands for the typical Na^+ intercalation/extraction processes into the carbon materials.[49] During the anodic process, the oxidation peaks appear at 1.53 and 1.76 V, which correspond to the formation of $CoSe_2$ and Fe_3Se_4. Compared to CSE and FSE, the CV curves of CFSE in the subsequent two cycling processes show relatively overlapped shapes, suggesting an excellent electrochemical reversibility and stability in CFSE.[27] Fig. S29 illustrates the galvanostatic charge/discharge (GCD) profiles of the CFSE electrodes for the initial

View Article Online
DOI: 10.1039/D6SC03276A

three cycles. For the first cycle, the specific charge/discharge capacities of the CFSE electrode are 484.3/499.1 mAh g^{-1}, with an initial Coulombic efficiency (ICE) of 97.1%, which is higher than that of CSE (191.6/200.4 mAh g^{-1}, 95.6%) and FSE (437.8/471.8 mAh g^{-1}, 92.8%). The results demonstrate excellent energy conversion efficiency and superior energy utilization rate of CFSE anodes.[40]

The cycle performance of CFSE, CSE, and FSE at a current density of 0.1 A g^{-1} is exhibited in Fig. 4h. The capacity of the CFSE electrode shows a gradual increase after the initial cycles, which is attributed to the gradual activation of active materials during the cycling process. After 200 cycles, the CFSE electrode achieves a higher reversible and stable capacity of 475.6 mAh g^{-1} than that of FSE (354.1 mAh g^{-1}, 173 cycles) and CSE (240.3 mAh g^{-1}). To get a profound understanding of the phase evolution of CFSE electrodes during repeated discharge and charge processes, differential specific capacity (dQ/dV) curves within the first 200 cycles at 0.1 A g^{-1} were illustrated in Fig. 4i and Fig. S30. During the discharging process of the CFSE electrode, a dQ/dV peak related to the insertion of sodium ions is detected at approximately 1.6 V. The intensity of this peak slightly weakens within the subsequent cycles, indicating that the non-Faradaic behavior gradually becomes predominant.[32] Conversely, the peak at 0.73 V shows a high and stable intensity within a narrow voltage range, indicating a continuous conversion reaction during discharge processes, with Faradaic behavior being predominant. During the charging process, the peaks are detected in the contour plot at 1.53 and 1.9 V, which stand for the reverse conversion reaction process and the extraction of Na^+ phase, respectively. As the cycle number

View Article Online
DOI: 10.1039/D6SC03276A

increases, the peak intensity at 1.9 V gradually strengthens, suggesting clearer charge platforms and a more prominent contribution of Faradaic behavior. This observation is likely associated with the structural reorganization of CFSE and gradual stabilization of charge transport during repeated cycling. The interface construction of heterostructure between $CoSe_2$ and Fe_3Se_4 can more effectively facilitate electrode materials activation and phase reorganization, as well as facilitate fast Na^+ diffusion kinetics. As shown in Fig. 4j, the CFSE electrode achieves reversible specific capacities of 461.7, 454.2, 442.0, 434.8, 422.3, 398.0, and 364.4 mAh g^{-1} from 0.1 to 10.0 A g^{-1}, respectively. When the current density switched back to 0.1 A g^{-1}, the specific capacity of CFSE can still be retained at 457.2 mAh g^{-1}. The corresponding GCD profiles of CFSE display well-maintained potential plateaus, suggesting that the electrode at various current densities possesses low polarization and faster reaction kinetics. In comparison, the CSE and FSE electrodes show inferior rate performance with poor capacity delivery and low capacity retention from 0.1 to 10.0 A g^{-1} due to increased voltage polarization and kinetic barriers (Fig. S31). In addition, it can be detected from Fig. S32 and Table S2 that the rate performance of the CFSE electrode is remarkably superior to earlier reported selenide heterostructure anode materials for SIBs, attributing to the synergistic effect of orbital coupling and spin modulation in the CFSE heterostructure. Moreover**,** long-term cycling performance assessment reveals that CFSE maintains a significant specific capacity of 395.8 mAh g^{-1} after 1200 cycles at 2.0 A g^{-1}, with a capacity retention of 94.4 %, surpassing both CSE (131.3 mAh g^{-1}) and FSE (167.3 mAh g^{-1}), as well as reported selenium-based heterojunction anodes

View Article Online
DOI: 10.1039/D6SC03276A

for SIBs (Fig. 4k,l, Fig. S33, and Table S3).

To further understand the excellent cyclic stability of the CFSE heterostructure, we conducted morphology characterization of the different anodes collected after 100 cycles at a current density of 1.0 A g^{-1}. For CSE and FSE, severe cracks and loosely stacked particles were detected on the entire surface of the electrode (Fig. S35a,b, and Fig. S36a,b), indicating that the SEI layer generated on the surface could be unstably maintained after continuous charge and discharge cycles. In contrast, the surface of CFSE remained a smooth and intact surface without obvious cracks (Fig. 5a and Fig. S34), thus achieving excellent cycle stability for efficient sodium storage. Moreover, the macroscopic changes of CFSE, CSE, and FSE electrodes were investigated by measuring their cross-sectional thicknesses. The initial thickness of the CFSE electrode was 8.7 μm, and after cycling the thickness increased to 10.8 μm, representing a volume expansion of 23% (Fig. 5b,c). In contrast, the volume variations of CSE (Fig. S35c,d) and FSE (Fig. S36c,d) anodes are much larger than that of the CFSE heterojunction during the repeated charging and discharging processes, which can explain the superior cycling life of the CFSE anodes.

We utilized HRTEM to explore the impact of heterostructure on the morphological and structural features of SEI. Specifically, the CFSE electrode retains a thinner and more homogeneous SEI film (~4 nm) after 10 cycles, compared with the thicker and more uneven SEI films detected on the CSE and FSE electrodes (Fig. 5d and Fig.S37). XPS measurements were conducted to further investigate the structure and composition of SEI on different electrodes after 10 cycles. As depicted in Fig. 5e, pristine CFSE

View Article Online
DOI: 10.1039/D6SC03276A

sample exhibits three primary peaks at approximately 284.6, 286.9, and 289.4 eV, which correspond to the C−C, C−O, and Na_2CO_3, respectively.[50, 51] After etching, the C 1s spectra peak related to Na_2CO_3 in CFSE shows remarkably lower intensity than those of CSE and FSE, indicating less decomposition of electrolyte (Fig. S38). This suggests the formation of stable SEI layers in CFSE.[50] Furthermore, the O 1s spectra analysis also demonstrates the existence of C−O and C=O bonds, which are attributed to the resolution of the ether-based electrolyte (Fig. S39). The cycled CFSE anode exhibits a lower peak intensity of oxygen species compared to CSE and FSE, inhibiting continuous electrolyte decomposition.[52] In addition, the F 1s spectra display the signals of Na−F (684.1 eV) and P−F (687.85 eV), which are attributed to the formation of NaF-rich SEI and residual sodium salt (Fig. 5f and Fig. S40).[53] As etching continued, the Na−F bond peaks became more prominent, indicating in-situ generation of a robust NaF-rich SEI inner layer. According to the atomic percentage analysis, the SEI layers of CFSE exhibit lower atomic percentages of O and higher fluorine content, demonstrating a thinner organic outer layer as well as a NaF-rich inorganic inner layer (Fig. 5i and Fig. S41). Notably, NaF exhibits a small Na^+ diffusion barrier and remarkable electronic insulation characteristics, which promote fast Na^+ migration inside the SEI, while significantly inhibiting electron penetration from the SEI layer.[5] These properties of the NaF- rich inorganic layer are conducive to the rapid charging capability of the CFSE anode and enable its stability in long-term cycling. Moreover, in the initial un-etched state after full sodiation, the signals for Co 2p of CFSE are not observed, which could be attributed to the formation of the NaF-

View Article Online
DOI: 10.1039/D6SC03276A

rich SEI layer (Fig. 5g,h,j). As etching proceeded, the intensities of Co^{2+} and Co^{3+} peaks were significantly strengthened and eventually maintained stable, indicating an obviously thinner SEI layer. The formation mechanism of SEI on the surface of the CFSE includes $NaPF_6$ decomposition into NaF and PF_5 at the anode-electrolyte interface. DFT calculations demonstrate that the dissociation energy barrier of $NaPF_6$ on CFSE is 0.32 eV, significantly lower than that of CSE (0.94 eV) and FSE (0.48 eV) (Fig. 5k-m). This result suggests that CFSE effectively promotes the P−F bond breaking in $NaPF_6$ and facilitates NaF nucleation through offering abundant active sites (Co and Se), which is beneficial to the generation of a robust SEI layer on the heterostructure (Fig. S42).

In summary, the Co^{2+} spin state transition from low-spin to high-spin at the heterojunction interface promotes more inorganic (inner: NaF) and less organic (outer layer) dual-layer SEI components. The unique and dense dual-layer SEI structure mitigates the continuous electrolyte consumption and interface side reactions with reduced gas evolution(i.e., the reaction path of i-ii) (Fig. S43).[54] Therefore, spin modulation enables achieve a thin and robust dual-layer SEI as well as high ionic conductivity due to the shorter diffusion pathway (Fig. S44), which contributes to achieving the stable cycling performances. As illustrated in Fig. 5n, the SEI generated in ether-based electrolyte exhibits a double-layer architecture, containing a dense NaF-rich inorganic inner layer and an organic outer layer. During the Na^+ insertion/extraction process, the organic outer layer ensures sufficient and stable Na^+ flux, facilitating rapid sodium storage kinetics. Additionally, the dense inorganic inner

View Article Online
DOI: 10.1039/D6SC03276A

layer dominated by NaF/Na_2CO_3 has a high modulus to resist severe volume variations and suppress excessive electrolyte decomposition, achieving the superior electrochemical performances.

Conclusion

In this study, we have elaborately designed and prepared CFSE heterostructures via a facile co-precipitation and selenization strategy. The systematic DFT calculations and experimental studies were adopted to explore the role of electronic-spin regulation and asymmetric orbital hybridization in the enhanced sodium storage performance of the CFSE composite. The CFSE shows a high spin state of Co, which contributes to energy level up-shift and activates more electronic states in 3*d* orbitals. The Co–Se–Fe asymmetric orbital hybridization at the heterointerface accelerates electron transfer from Fe to Co, which results in the upshift in the ε_d of Co. This enhances the adsorption energy and lowers the diffusion barrier of sodium ions. Furthermore, the synergetic spin-orbital modulation in CFSE heterostructure reduces the dissociation energy barrier of $NaPF_6$, thereby tailoring a stable, thin, and NaF-rich SEI layer, which is conducive to sustained long cycle life of SIBs. Consequently, compared with CSE and FSE, CFSE achieves longer cycle life (395.8 mAh g^{-1} after 1200 cycles with a capacity retention of 94.4%). This study highlights the critical roles of spin engineering and orbital hybridization in heterostructure materials, which can offer guidance for developing other conversion-type anodes for high-performance SIBs.

View Article Online
DOI: 10.1039/D6SC03276A

Data availability

Data will be made available on request.

Conflicts of interest

There are no conflicts of interest to declare.

Acknowledgements

This work was supported by the National Natural Science Foundation of China (52502298, 52302240), the Macao Young Scholars Program (AM2023011), the Yuanguang Scholars Program, Hebei University of Technology (282022554).

Author contributions

Mingyu Lian: Investigation, Formal analysis, Data curation, Writing–original draft, Writing–review & editing. **Yitong Sun:** Investigation, Formal analysis, Data curation, Writing–original draft, Writing–review & editing. **Di Zhou:** Data curation, Formal analysis, Writing–review & editing. **Yijia Zhang:** Data curation, Formal analysis, Writing–review & editing. **Qingqing Zhou:** Data curation, Writing–review & editing. **Ying Jiang:** Software, Validation, Funding acquisition, Project administration, Resources, Supervision, Writing–review & editing. **Zhengqing Ye:** Conceptualization, Funding acquisition, Investigation, Methodology, Project administration, Resources, Supervision, Writing–review & editing.

View Article Online
DOI: 10.1039/D6SC03276A

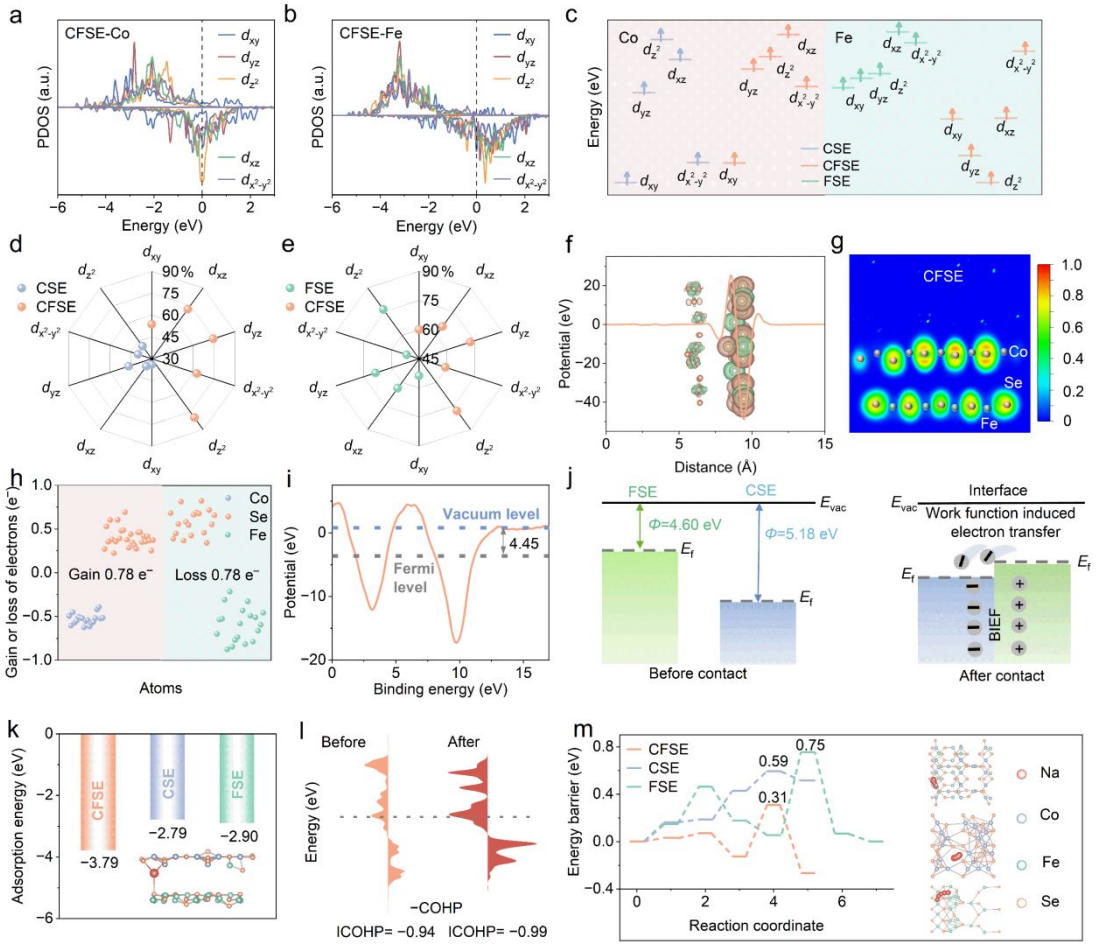

Fig. 1 a) The PDOS of Co-*d* orbitals and b) Fe-*d* orbitals in CFSE. c) Schematic diagram of the energy levels of Co-*d* and Fe-*d* orbitals. d,e) Spin polarizability of splitting 3*d* orbitals of various samples. f) Charge density difference of the heterointerface in CFSE and corresponding planar average charge density difference in the Z direction. g) The Electron Localization Function (ELF) of CFSE. h) Electron gain/loss of different atoms calculated by Bader charge analysis. i) The work function of CFSE. j) Schematic diagram of electron redistribution at the heterointerface between FSE and CSE. k) Na^+ adsorption energy. l) COHP plots and corresponding ICOHP values of CFSE before and after Na insertion. m) The top views of diffusion pathways and diffusion barriers

View Article Online
DOI: 10.1039/D6SC03276A

of Na^+ in CFSE, CSE, and FSE.

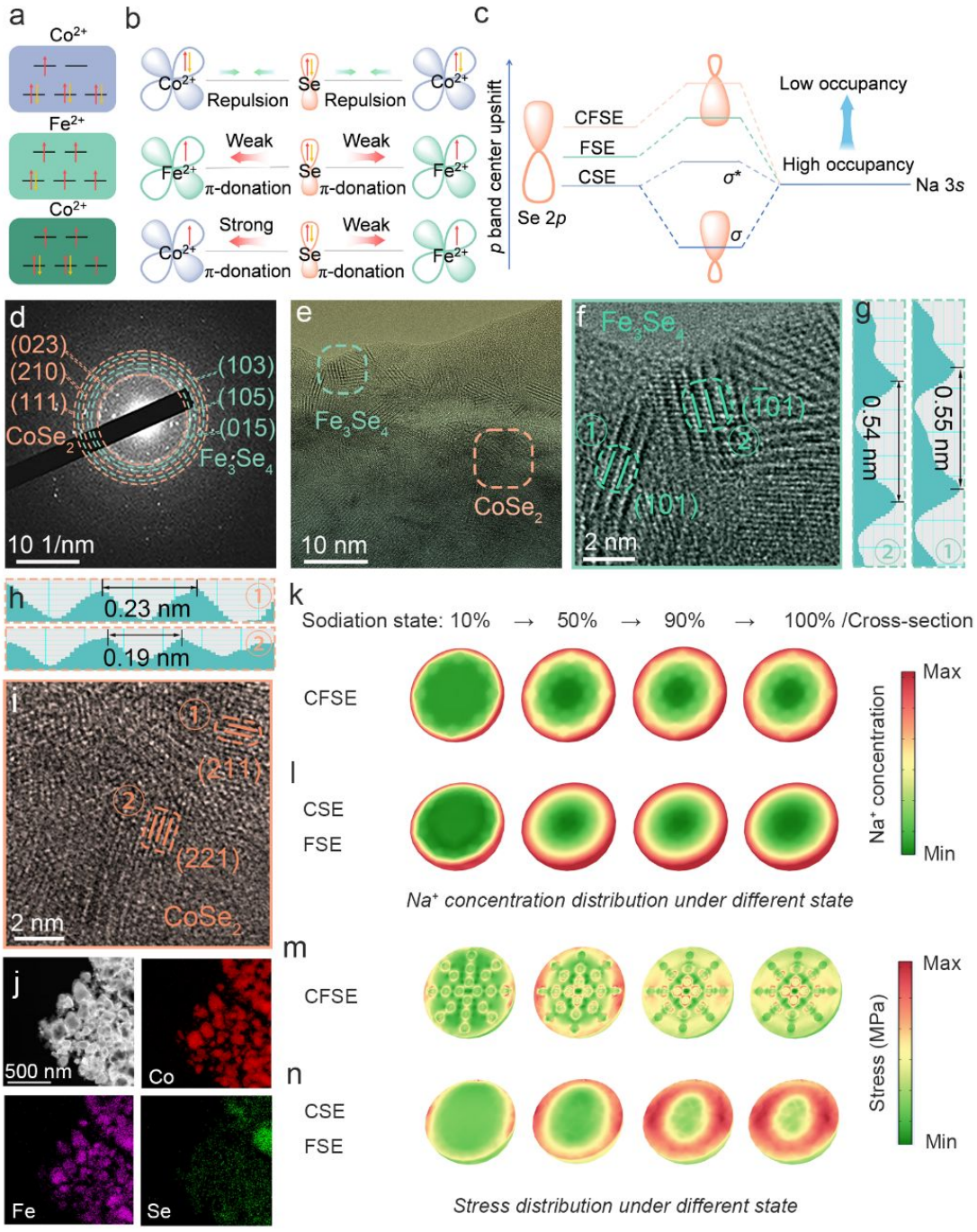

Fig. 2 a) Schematic illustration of the energy level splitting of *d* orbitals of different metal ions. b) Illustration of electronic interaction on the t_{2g} orbital for CSE, FSE, and CFSE. c) Schematic illustration of the *p* band center modulation and Na−Se interaction. d) SAED pattern of CFSE. e,f,i) HRTEM image and g,h) FFT lattice images of the

View Article Online
DOI: 10.1039/D6SC03276A

selected areas of CFSE. j) HAADF-STEM image and corresponding elemental mapping of CFSE. The Na^+ concentration and stress distribution of k,m) CFSE model and l,n) CSE or FSE model of sodiation states at 10%, 50%, 90%, and 100%, respectively.

View Article Online
DOI: 10.1039/D6SC03276A

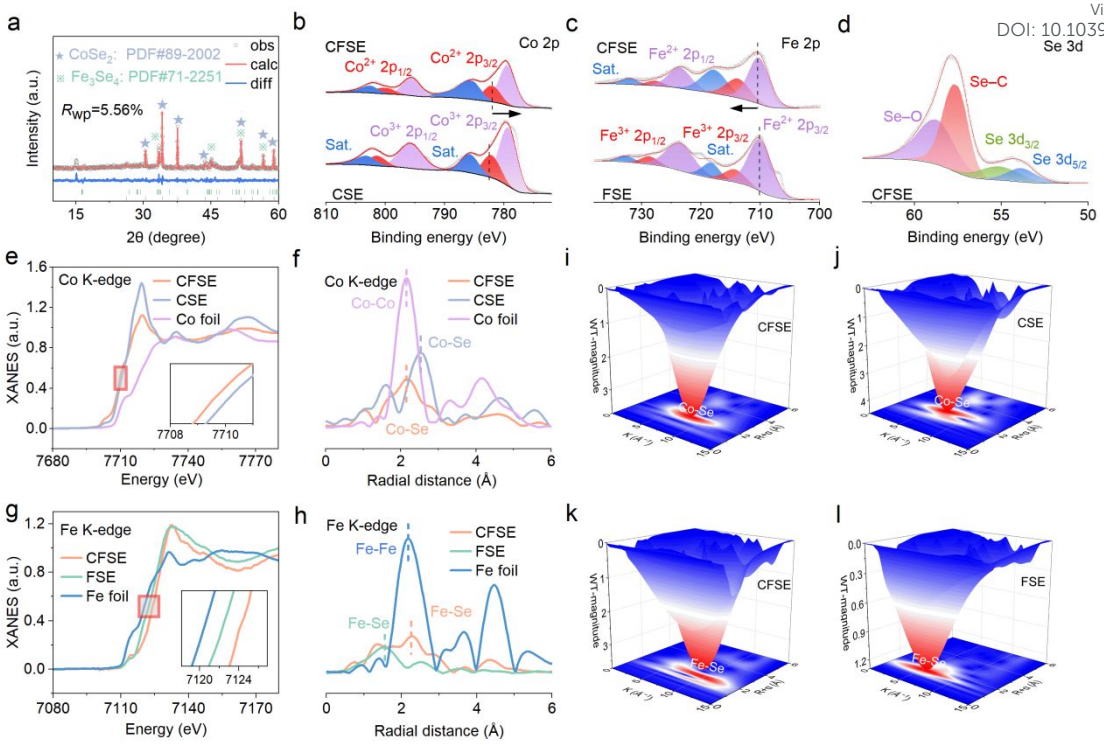

Fig. 3 a) XRD pattern of CFSE. High-resolution XPS spectra of b) Co 2p, c) Fe 2p, d) Se 3d. e) Co K-edge XANES spectra. f) Co K-edge FT-EXAFS spectra. g) Fe K-edge XANES spectra. h) Fe K-edge FT-EXAFS spectra. WT contour plots of Co K-edge in i) CFSE, j) CSE, and Fe K-edge in k) CFSE and l) FSE.

View Article Online
DOI: 10.1039/D6SC03276A

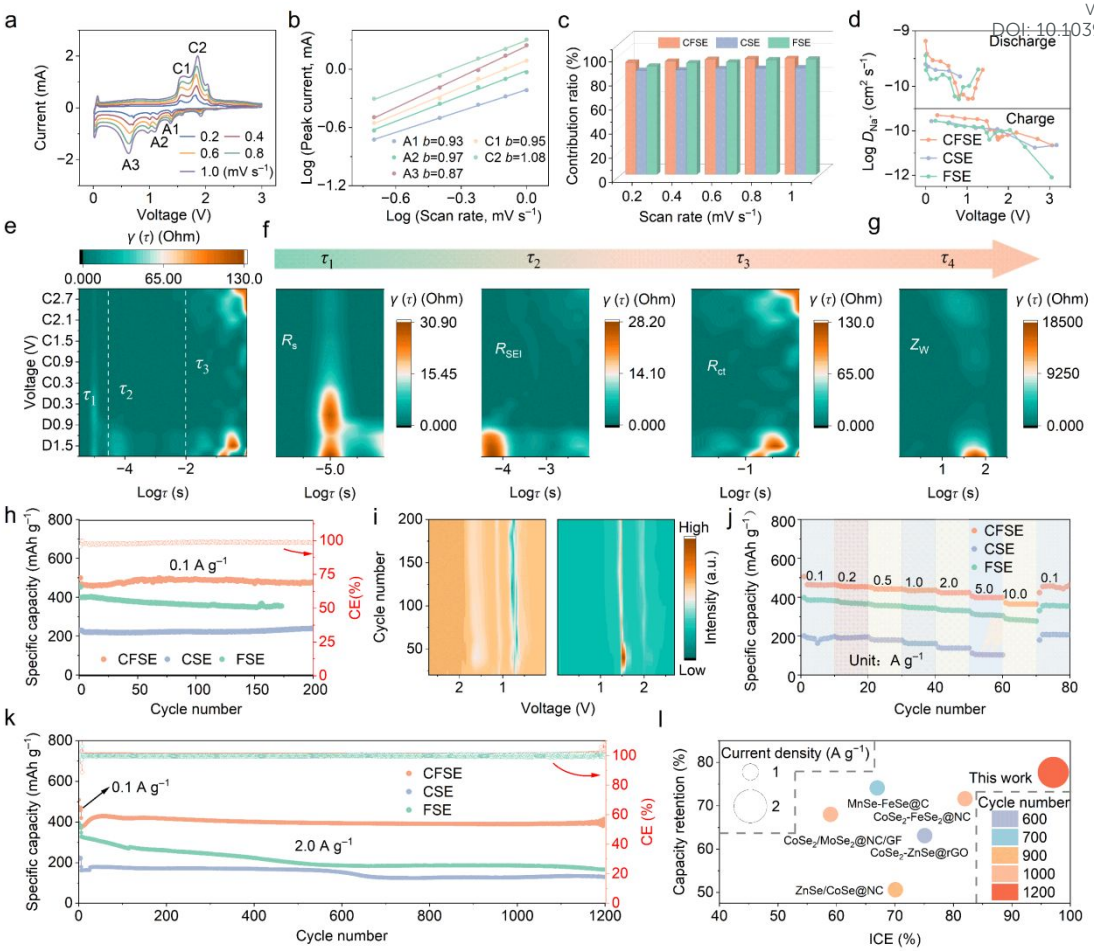

Fig. 4 a) The CV curves of CFSE at different scanning rates. b) The fitting curves and corresponding *b* values of each marked peak in a) from the logarithmic values of different peak currents and scan rates. c) Contribution ratios of capacitive behaviors at various scan rates for CFSE, CSE, and FSE. d) Diffusion coefficient for CFSE, CSE, and FSE during discharge and charge processes. e-g) 2D DRT intensity mapping originating from in-situ EIS measurements during the first discharge and charge processes of CFSE. h) Cyclic performance at 0.1 A g^{-1}. i) 2D dQ/dV contour plot of CFSE during the 200 cycles. j) Rate performance. k) The long-term cyclic performance of CFSE, CSE, and FSE at 2.0 A g^{-1}. l) Comparison of long-term cycling performance of CFSE with other conversion anode materials for SIBs.

View Article Online
DOI: 10.1039/D6SC03276A

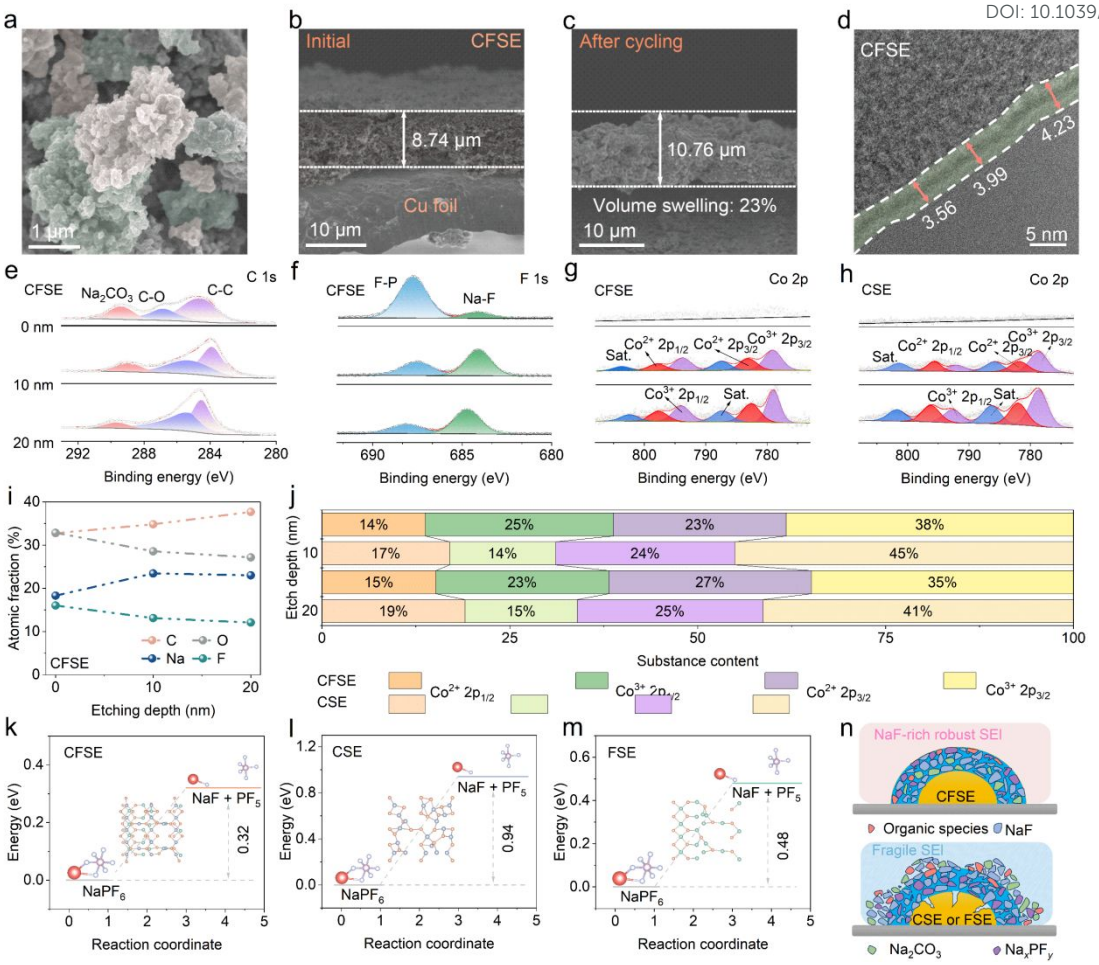

Fig. 5 The chemical and mechanical stability of CFSE. a) SEM image of CFSE after cycling. Cross-sectional SEM images of CFSE b) before and c) after cycling. HRTEM images of d) CFSE electrode at 0.1 A g^{-1}. XPS spectra of e) C 1s, f) F 1s, and g) Co 2p in CFSE electrodes after the 10th cycles. h) Co 2p XPS of CSE after the 10th cycles. i) Atomic fraction of C, O, F, and Na after different etching depths. j) Various Co spin state percentage of CFSE and CSE at different etch depths. The energy illustration of $NaPF_6$ decomposition to NaF and PF_5 on the surfaces of k) CFSE, l) CSE, and m) FSE. n) Schematic illustration of the SEI structure formed on CFSE and CSE (FSE).

View Article Online
DOI: 10.1039/D6SC03276A

References

1 Y. Sun, G. Åvall, S.-H. Wu, G. A. Ferrero, A. Freytag, P.B. Groszewicz, H. Wang, K.A. Mazzio, M. Bianchini, V. Baran, S. Risse, P. Adelhelm, *Nat. Mater.,* 2025, **24**, 1441-1449.

2 Skurtveit, A. Pastusic Jr, A. Brennhagen, F.M. Maddar, C.E. Mohn, A. Karmakar, C.A. O'Keefe, I. Hasa, C. Cavallo, B. Arstad, H. Fjellvåg, D.S. Wragg, A.Y. Koposov, *Adv. Energy Mater.,* 2025, **15**, 2501433.

3 Z. Hong, Z.-C. Jian, Y.-F. Zhu, Y.-J. Li, Q.-C. Ling, H. Xin, D. Wang, C. Wu, Y. Xiao, *Chem. Sci.,* 2025, **16**, 17058-17085.

4 J. Zong, Y. Liang, F. Liu, M. Zhang, K. Song, J. Feng, B. Xi, S. Xiong, *Nat. Commun.,* 2025, **16**, 4406.

5 S. Zhang, W. Zuo, X. Fu, J. Li, Q. Zhang, W. Yang, H. Chen, J. Zhang, X. Xiao, K. Amine, S.-G. Sun, F. Fu, M. Ye, G.-L. Xu, *Nat. Commun.,* 2025, **16**, 4052.

6 Z. Sun, J. Zhang, J. Zhang, C. Zhang, J. Han, Z. Sun, H. Yang, J. Pan, X. Wu, S. Feng, H. Yang, W. Chen, L. Zhang, D.-L. Peng, Q. Zhang, *Adv. Mater.,* 2025, **38**, e17606.

7 J. Qin, X. Wang, H. Li, F. Wang, L. Chen, H. Miao, F. Xing, S. Yuan, Z. Ye, X. Li, X. He, *ACS Nano*, 2025, **19**, 32322-32334.

8 J. Ning, M. Zhou, Y. Zhang, T. Wang, M. Chen, Q. Cu, K. Wang, W. Wang, H. Li, K. Jiang, *EcoEnergy*, 2025, **3**, e70006.

9 H.-Y. Hu, J.-Y. Li, Y.-F. Liu, Y.-F. Zhu, H.-W. Li, X.-B. Jia, Z.-C. Jian, H.-X. Liu, L.-Y. Kong, Z.-Q. Li, H.-H. Dong, M.-K. Zhang, L. Qiu, J.-Q. Wang, S.-Q. Chen,

View Article Online
DOI: 10.1039/D6SC03276A

X.-W. Wu, X.-D. Guo, Y. Xiao, *Chem. Sci.,* 2024, **15**, 5192-5200.

10 Y. Feng, Y. Li, X. Xu, Z. Bu, J. Yin, D. Yang, J. Liu, L. Qin, K. Li, F. Wang, Y. Zhou, L. Zhou, Y. Chang, J. Li, D.-Y. Chen, Q. Li, *Adv. Funct. Mater.,* 2025, **35**, 2500234.

11 X. Li, Q. Zhang, R. Wang, J. Huang, J. Han, T. Yao, X. Wang, S. Jiang, B. Song, *Adv. Funct. Mater.,* 2026, e28353. DOI: 10.1002/adfm.202528353

12 F. Liu, J. Zong, Y. Liang, M. Zhang, K. Song, L. Mi, J. Feng, S. Xiong, B. Xi, *Adv. Mater.,* 2024, **36**, 2403131.

13 Z. Huang, G. Wang, S. Xie, W. Zhang, J. Wang, Z. Lin, G. Wang, H. Chu, Y. Zhong, Y. Huang, J. Xu, S. Xiong, S. Huang, *Adv. Funct. Mater.,* 2025, **35**, 2424278.

14 P. Song, J. Yang, C. Wang, T. Wang, H. Gao, G. Wang, J. Li, *Nano-Micro Lett.,* 2023, **15**, 118.

15 Y. Jiang, M. Lian, J. Ma, Y. Long, X. Guo, Y. Sun, J. Lao, Z. Ye, *Nano Lett.,* 2025, **25**, 7241-7248.

16 H. Peng, W. Miao, J. Zeng, Z. Wang, C. Yan, G. Ma, Z. Lei, *Adv. Sci.,* 2025, **12**, 2417288.

17 M. Chen, S. Gu, J. Li, Y. Dai, Y. He, B. Sun, T. Gao, L. Xu, G. Zhou, *Adv. Sci.,* 2025, **12**, e09997.

18 Q. Li, Z. Liang, Y. Huang, W. Zhang, S. Xie, Y. Zhong, C. Zhao, Z. Luo, S. Huang, *Adv. Mater.,* 2025, **37**, 2502894.

19 Lu, B. Li, M. Shi, Q. Li, K. Liu, C. Lu, J. Liao, Z. Hu, X. Wei, C. Li, Y. Sun, T.

View Article Online
DOI: 10.1039/D6SC03276A

Liu, R. Liu, Q. Zhao, *Adv. Energy Mater.,* 2025, **15**, 2405706.

20 H. Yang, D. Li, Z. Huang, H. Gao, Y. Ma, J. Ye, *Adv. Funct. Mater.,* 2025, **35**, e12226.

21 J. Wang, D. Zhang, Q. Wang, Q. Sun, H. Sun, Z. Li, H.J. Woo, S. Ramesh, B. Wang, *Adv. Funct. Mater.,* 2024, **34**, 2400261.

22 T. Feng, F. Wang, Z. Sun, F. Guo, Y. Xiong, F. Ren, C. Tang, J. Li, H. Kun Liu, S. Xue Dou, *Angew. Chem. Int. Ed.,* 2025, **64**, e202420504.

23 N. Shi, X. Li, G. Liu, Y. Liang, C. Sun, X. An, B. Xi, S. Xiong, *Small*, 2025, **21**, 2412304.

24 J. Ge, M. Huang, C. Li, X. Ji, X. Meng, H. Tan, H. Liu, W. Zhou, *Adv. Energy Mater.,* 2025, **15**, 2405288.

25 J. Li, Y. He, Y. Dai, H. Zhang, Y. Zhang, S. Gu, X. Wang, T. Gao, G. Zhou, L. Xu, *Adv. Funct. Mater.,* 2024, **34**, 2406915.

26 R. Xu, L. Wang, X. Yang, X. Li, Y. Jiang, W. Lü, *Small*, 2025, **21**, 2409423.

27 Y. Li, W. Li, M. Zhang, Y. Zhuang, H. Li, Z. Pan, H. Min, T.-Y. Chen, H.-Y. Chen, H. Yang, J. Wang, *Small*, 2024, **20**, 2405819.

28 S. Iqbal, A.N. Chishti, M. Ali, M. Ali, Y. Hao, X. Wu, H. Huang, W. Lu, P. Gao, M. Yousaf, Y. Jiang, *Small*, 2024, **20**, 2308262.

29 Y. Shi, Z.-R. Ma, Y.-Y. Xiao, Y.-C. Yin, W.-M. Huang, Z.-C. Huang, Y.-Z. Zheng, F.-Y. Mu, R. Huang, G.-Y. Shi, Y.-Y. Sun, X.-H. Xia, W. Chen, *Nat. Commun.,* 2021, **12**, 3021.

30 Z. Wang, W. Huang, H. Wu, Y. Wu, K. Shi, J. Li, W. Zhang, Q. Liu, *Adv. Funct.*

View Article Online
DOI: 10.1039/D6SC03276A

Mater., 2024, **34**, 2409303.

31 T. Yan, H. Hu, J. Duan, C. Zhu, Y. Wang, J. Wen, L. Li, Z. Xu, T. Wen, P. Yang, Z. Chen, *Chem. Eng. J.,* 2024, **499**, 155871.

32 T. Liu, Z. Wang, J. Luo, L. Li, X. Wang, C. Li, C. Zhu, D. Li, *Energy Storage Mater.,* 2025, **75**, 104044.

33 S. Yao, S. Wang, Y. Liu, Z. Hou, J. Wang, X. Gao, Y. Sun, W. Fu, K. Nie, J. Xie, Z. Yang, Y.-M. Yan, *J. Am. Chem. Soc.,* 2023, **145**, 26699-26710.

34 Y. Li, X. Wen, Y. Li, Y. Jiang, X. Li, Z. Du, H. Sun, Y. Peng, L. Song, R. Xu, L. Huang, C. Xiao, J. Shi, *Adv. Mater.,* 2025, **37**, 2506071.

35 L. Song, S. Zhang, L. Duan, R. Li, Y. Xu, J. Liao, L. Sun, X. Zhou, Z. Guo, *Angew. Chem. Int. Ed.,* 2024, **63**, e202405648.

36 Wang, Y. Chao, K. Guo, Z. Wang, M. Yang, J. Zhu, X. Cui, Q. Xu, *Adv. Funct. Mater.,* 2024, **34**, 2405642.

37 H. Zheng, D. Deng, X. Zheng, Y. Chen, Y. Bai, M. Liu, J. Jiang, H. Zheng, Y. Wang, J. Wang, P. Yang, Y. Xiong, X. Xiong, Y. Lei, *Nano Lett.,* 2024, **24**, 4672-4681.

38 Z.-H. Sun, D.-Y. Qu, D.-X. Han, Z.-Y. Gu, J.-Z. Guo, X.-X. Zhao, Y.-M. Ma, B.-L. Zhao, Z.-Q. Song, X.-L. Wu, L. Niu, *Adv. Mater.,* 2024, **36**, 2308987.

39 X. Xu, S. Chen, F. Liu, R. Wang, A.V. Trukhanov, Z. Sun, *Appl. Catal. B Environ. Energy*. 2026, **392**, 126726.

40 X. Wang, X. Du, J. Luo, L. Li, L. Tan, W. Dong, D. Li, Z. Guo, *Adv. Mater.,* 2024, **36**, 2407492.

41 B. Haruna, L. Wang, X. Hu, G. Luo, M.A. Muhammad, Y. Liu, J. Yu, A. Abdel-Aziz, H. Bao, Z. Wen, *Adv. Funct. Mater.,* 2025, **35**, 2414246.

42 Huang, J. Yu, Y.-J. Lei, O. Usoltsev, L. Gong, Z. Cui, J. Li, C. Li, B. Nan, X. Lu, R. He, X. Qi, Q. Xue, J. Chai, Y. Ren, X. Bi, Y. Cheng, J.Y. Zhou, A. Skorynina, A. Bugaev, P.R. Martínez-Alanis, L. Balcells, J. Arbiol, C.Y. Zhang, A. Cabot, *Chem. Eng. J.,* 2025, **506**, 160146.

43 Zhang, H. Xu, *Battery Energy*, 2024, **3**, 20230032.

44 Y. Sun, M. Lian, X. Guo, J. Ma, K. Liu, Z. Ye, X. Zhang, Y. Jiang, L. Zhang, *J. Energy Chem.,* 2026, **112**, 435-443.

45 C. Shi, D. Muhtar, Y. Pei, X. Lu, F. Liu, D. Wang, X. Lu, Z. Sun, *Adv. Energy Mater.,* 2026, e70898. DOI:10.1002/aenm.70898

46 S. Zhou, Z. Mao, J. Lin, J. Zhou, J. Liu, X. Shi, J. Xu, L. Shao, Z. Sun, *eScience Energy*, 2025, **1**, 100007.

47 Z. Chen, T. Tao, C. Shi, X. Shi, L. Shao, J. Xu, Z. Sun, *Carbon Neutralization*, 2025, **4**, e70010.

48 Y. Liu, Q. Hu, Q. Shi, S. Zhao, X. Hu, W. Feng, J. Xu, J. Zhang, Y. Zhao, *Adv. Energy Mater.,* 2025, **15**, 2500723.

49 D.-Y. Qu, Q.-Y. Li, Z.-H. Sun, C.-Y. Wei, Z.-Y. Gu, X.-X. Zhao, B.-L. Zhao, D.-X. Han, L. Niu, X.-L. Wu, *Adv. Funct. Mater.,* 2025, **35**, 2421504.

50 S.K. Kang, M. Kim, G.H. Park, J. Ji, S. Hong, W.B. Kim, *Adv. Funct. Mater.,* 2025, **35**, 2408986.

51 Y. Gong, Y. Li, Y. Li, M. Liu, X. Feng, Y. Sun, F. Wu, C. Wu, Y. Bai, *Nano Lett.,*

View Article Online
DOI: 10.1039/D6SC03276A

2024, **24**, 8427-8435.

52 L. Wang, Y. Fan, Y. Zhao, Q. Yuan, H. Ben, H. Xiong, Y. Shao, C. Lin, C. Ma, *Nano Energy*, 2024, **132**, 110408.

53 Chen, J. Zhu, T. Li, L. Liu, J. Zou, Z. Wang, Y. Chao, X. Cui, W. Chen, *Energy Storage Mater.,* 2025, **79**, 104349.

54 J. Luo, K. Yang, J. Gai, X. Zhang, C. Peng, C. Qin, Y. Ding, Y. Yuan, Z. Xie, P. Yan, Y. Cao, J. Lu, W. Chen, *Angew. Chem. Int. Ed.,* 2025, **64**, e202419490.

View Article Online
DOI: 10.1039/D6SC03276A

Data availability

The data that support the findings of this study are available from the corresponding author upon reasonable request.